Nanoscale

PAPER

View Article Online
View Journal

Cite this: DOI: 10.1039/d1nr06121f

Bulk and surface exsolution produces a variety of Fe-rich and Fe-depleted ellipsoidal nanostructures in $La_{0.6}Sr_{0.4}FeO_3$ thin films†

Komal Syed, [a] Jiayue Wang, [b] Bilge Yildiz [b,c] and William J. Bowman *[a,d]

The past several years have seen a resurgence in the popularity of metal exsolution as an approach to synthesize advanced materials proposed for novel catalytic, magnetic, optical, and electrochemical properties. Whereas most studies to-date have focused on surface exsolution (motivated by catalysis), we instead report on the diversity of nanostructures formed in $La_{0.6}Sr_{0.4}FeO_3$ thin films during sub-surface or so-called 'bulk' exsolution, in addition to surface exsolution. Bulk exsolution is a promising approach to tuning the functionality of materials, yet there is little understanding of the nanostructures exsolved within the bulk and how they compare to those exsolved at gas–solid interfaces. This work combines atomic- and nano-scale imaging and spectroscopy techniques applied using a state-of-the-art aberration-corrected scanning transmission electron microscope (STEM). In doing so, we present a detailed atomic-resolution study of a range of Fe-rich and Fe-depleted nanostructures possible *via* exsolution, along with qualitative and quantitative chemical analysis of the exsolved nanostructures and oxide phases formed throughout the film. Local structural changes in the perovskite matrix, coinciding with nanostructure exsolution, are also characterized with atomic-resolution STEM imaging. Fe exsolution is shown to create local A-site rich domains of Ruddlesden–Popper phase, and some stages of this phase formation have been demonstrated in this work. In particular, phase boundaries are found to be the primary nucleation sites for bulk and surface exsolution, and the exsolved particles observed here tend to be ellipsoidal with shape factor of 1.4. We report a range of nanostructure types (core–shell, bulk core–shell, adjacent, and independent particles), revealing several possible avenues of future exploration aimed to understand the formation mechanism of each exsolution type and to develop their functionality. This work is thus relevant to materials scientists and engineers motivated to understand and utilize exsolution to synthesize materials with predictable nanostructures.

Received 17th September 2021,
Accepted 30th November 2021

DOI: 10.1039/d1nr06121f

rsc.li/nanoscale

Introduction

Exsolution is an *in situ* synthesis method for creating highly-tunable catalytic nanostructures anchored in the surface of an oxide support.[1–7] This flexible nanocatalyst synthesis approach can produce active particles which are more durable than impregnated nanostructures, and which can be strained as a result of being partially submerged in the oxide – offering enhanced activity. Our current understanding of exsolution results from nearly two decades of catalysis research dating back to pioneering work on "self-regenerative" perovskite-supported precious metal (Pd, Rh and Pt) catalysts for automotive emissions control by researchers at Daihatsu.[1,8–12] Since then, a range of nanostructures have been developed for several catalytic applications, such as solid oxide fuel/electrolysis cells,[4,5,13–29] hydrogen and syngas production,[18,30–34,35–37] oxygen evolution,[38] CO_2 reduction,[39,40] and photocatalysis.[41] Very recently, focus has turned to engineering the bulk properties of functional oxides using the bulk exsolution design strategy, which, for instance have effectively tailored the electronic transport properties of a lanthanum ferrite perovskite.[42]

Exsolution, also called "self-regeneration" or "solid-state crystallization" is a phase decomposition reaction that involves metal cation coalescence at/near individual atomic-scale point defects of opposite charge, such as oxygen vacancies. This is often observed in the vicinity of extended defects like surfaces

[a]Department of Materials Science & Engineering, University of California, Irvine, CA, USA. E-mail: will.bowman@uci.edu
[b]Department of Nuclear Science and Engineering, Massachusetts Institute of Technology, Cambridge, MA, USA
[c]Department of Materials Science and Engineering, Massachusetts Institute of Technology, Cambridge, MA, USA
[d]Irvine Materials Research Institute, University of California, Irvine, CA, USA

†Electronic supplementary information (ESI) available. See DOI: 10.1039/d1nr06121f

and grain boundaries due to the relatively lower vacancy formation energy. Li, Liu *et al.* reviewed progress in the field of exsolution-derived electrocatalysts through 2017, see Table 3 of ref. 2. Many compositions have been investigated, mainly with the goal of efficient use of precious metals and various transition metals (though mostly Ni or its alloys) selected for particular reactions. Transition metals (MnO,[3,26,43] Fe,[3,13,28,30,43–45] Fe–Co,[29] $FeNi_3$,[40] Fe–Ni,[17,30] Co,[24,25,43,46] Co–Ni,[25,47] Ni,[4,5,13–16,18,22,24,25,27,31–37,43,48–50] Ni–Cu,[32] Cu,[3,24,32] Re/Ni/Fe,[51] Ce,[3] Ag,[19] Rare-earth vanadates doped with transition metal[24]), noble metals (Pd,[1,10–12,23] Pt,[9,10,12,52] Ir,[38] Rh,[9,10,12,39,52,53] Ru[20–22]), and transition metal dichalcogenides (WS_2 [41]) have been widely studied for exsolution.

In terms of nanostructure morphology, the main focus has been surface-anchored nanostructures for catalysis; however, several researchers have also reported bulk (*i.e.*, sub-surface) exsolution of embedded nanostructures.[54–56] Dai, Pan, *et al.* concluded based on *in situ* TEM studies of Rh exsolution from $CaTiO_{3-\delta}$ that initial-stage exsolution created nanostructures embedded in the perovskite matrix, making them inaccessible during heterogeneous catalysis.[53] Kim, Choi, *et al.* reported STEM dark field images clearly showing bulk exsolution of Ni particles throughout the thickness of epitaxially grown $La_{0.2}Sr_{0.7}Ti_{0.9}Ni_{0.1}O_{3-\delta}$ thin films, but did not interrogate these nanostructures beyond nanometer-scale energy dispersive spectroscopy (EDS) line profiles confirming the presence of Ni.[50] Han, Irvine, *et al.* showed as well that Ni exsolves in the bulk of epitaxial $La_{0.2}Sr_{0.7}Ni_{0.1}Ti_{0.9}O_{3-\delta}$ thin films, and while they did not explore this, there is indication that various core–shell nanostructures formed in their films during/after Ni exsolution.[37] In the context of bulk exsolution, Kousi, Metcalfe, *et al.* demonstrated that submerged Ni nanoparticles exsolved from $La_{0.8}Ce_{0.1}Ni_{0.4}Ti_{0.6}O_{3-\delta}$ strain the perovskite lattice upon oxidation to crystallographically-aligned NiO, yielding favorable oxygen exchange properties for methane conversion to syngas.[34]

Recent publications by co-authors of this study have been focused on Fe exsolution in $La_{0.6}Sr_{0.4}FeO_3$ (LSF) thin films.[6,42] Most recently, Wang *et al.* reported that Fe^0 exsolution in LSF results in major chemical and structural reorganization at the surface and also in the bulk, which can be used effectively to tailor electrical, magnetic and chemical properties of the resulting nanocomposite.[42] It was demonstrated that exsolution in LSF results in not only metallic iron nanoparticles whose magnetization could be modulated, but also Ruddlesden–Popper domains and Fe-deficient percolating channels which facilitated an increase in electronic conductivity by over 100 times.[42] Particularly, it was shown that the Fe-deficient percolating channels can enhance electronic conductivity by several orders of magnitude.[42] Such findings have direct implications for fabricating multifunctional nanocomposites for wide range of applications, making this LSF system valuable for exploring bulk and surface nanostructure morphology.

Here, we report a detailed-study of various Fe-based embedded nanostructures possible in LSF thin films *via* so-called bulk exsolution. LSF was chosen as a model perovskite system due to well-understood defect chemistry and the technological promise provided by its bulk properties in chemical looping, solid oxide cells, and facilitating magnetic nanostructures, as described in our recent study[42] which also includes discussion of the formation mechanism of the exsolved nanostructures in some detail. The aim of this work is to illustrate the variation in nanostructures that one can make in this material, which should help guide the design and synthesis of exsolved nanostructures in a broad range of chemical compositions, microstructures, and applications. We quantify the structural and chemical aspects of bulk exsolution using imaging and spectroscopy down to the atomic- and nanoscale using a state-of-the-art aberration-corrected STEM. There has not yet been a detailed study on the various types of nanostructures possible *via* bulk exsolution.

William J. Bowman

William J. Bowman is an Assistant Professor of Materials Science and Engineering at the University of California, Irvine. His lab focuses on understanding and developing oxide ceramics and nanomaterials for electrochemical energy conversion and storage, and CO_2 capture, and performs material synthesis, property testing, and multiscale characterization primarily using electron microscopy. His research has been funded by the National Science Foundation, the American Chemical Society, and the Research Corporation for Science Advancement. He has received the NSF CAREER award, the NSF Graduate Research Fellowship, the Swiss Government Excellence Scholarship, and the Microscopy Society of America Presidential Scholar Award.

Methods

LSF thin films were synthesized by PLD

LSF powders were prepared by mixing and grinding La_2O_3 (Sigma Aldrich, 99.999%), $SrCO_3$ (Sigma Aldrich, 99.995%), and Fe_2O_3 (Alfa Aesar, 99.998%) powders in appropriate ratios, and then being calcined at 1000 °C for 5 hours. The powders are then pressed into a pellet with a hydrostatic press and sintered at 1350 °C for 20 hours in stagnant air, thus yielding the target.

MgO (001) single crystal substrates (MTI Corporation, 1-side polished) were employed in this work. During pulsed laser deposition (PLD), the substrate temperature was kept at 850 °C in an oxygen pressure of 20 mTorr. By applying 30 000 laser pulses (laser energy: 400 mJ) to the LSF target, an LSF thin film of ~120 nm thickness was grown on the substrate (sub-

strate to target distance is 85 mm). This LSF film before exsolution will be referred to as 'as-prepared LSF' for rest of the article. After deposition, the sample was cooled in the deposition atmosphere at a cooling rate of 5 °C min^{-1}.

Fe exsolution was induced by exposure to H_2

LSF sample is reduced in 0.5 Torr flushing H_2 at 400 °C for 0.5 hours to trigger exsolution.

Atomic-scale imaging and chemical analyses were performed by aberration-corrected STEM – energy dispersive spectroscopy (EDS)

Exsolution in LSF was characterized using state-of-the-art aberration corrected JEOL Grand ARM300CF STEM operated at 300 keV. This instrument is equipped with dual silicon drift detectors for EDS with total detector area of 200 mm^2. The probe size was ~0.1 nm with a probe current of about 35pA. Low-background, high count analytical TEM holder was used to minimize any stray X-rays caused by holder. The film thickness of the exsolved LSF film (on MgO substrate) used in this study was measured to be ~165 nm.

Gatan Microscopy Suite (GMS version 3) software was utilized for STEM-EDS mapping and analysis using the following EDS peaks: O K_α (0.52 keV), Fe K_α and K_β (6.40 keV and 7.06 keV respectively), La L_α and L_β (4.65 keV and 5.04 keV and respectively), and Sr K_α and K_β (14.16 keV and 15.84 keV respectively). Net counts for EDS elemental maps were obtained after doing background subtraction using Kramers filter (with scaling option available in Gatan to better align the measured background to the original data). Due to sample drift observations during some EDS scans, aspect ratio for the EDS maps was accordingly adjusted to match the original STEM image.

To interpret the chemistry of exsolved nanostructures in LSF, Cliff–Lorimer method[57–59] was used to calculate concentrations of cations, Fe, La and Sr. Due to the widely known limitations of quantification of light elements by EDS, we excluded O from quantitative analysis in this study. Experimental *k*-factors were calculated using the as-prepared LSF film as reference, since the stoichiometric composition of homogeneous LSF film is known.

Additional physical, chemical, and functional characterization methods (atomic force microscopy, X-ray diffraction, X-ray photoelectron spectroscopy, X-ray absorption spectroscopy, electrochemical impedance spectroscopy, finite element analysis, and vibrating-sample magnetometry) are detailed elsewhere.[42]

Results and discussion

STEM-EDS characterization of bulk and surface nanostructures

The variety of nanostructures formed in LSF *via* exsolution are comprised of Fe-rich and Fe-depleted regions, accompanied by variation in La and Sr content (Fig. 1).[42] Using STEM high-angle annular dark field (HAADF) and bright field (BF) imaging, we characterized LSF film on (001) MgO substrate before (Fig. 1a–c) and after exsolution (Fig. 1d–f). After the treatment to trigger exsolution, LSF film shows distinct variety of nanostructures and oxide phases formed throughout the film (Fig. 1d–f). We also observe the formation of Ruddlesden–Popper (RP) phase after exsolution; RP is a perovskite-like derivative with A-site rich domains and is quantified by a local translation of the $ABO_{3-\delta}$ structure by sqrt($\frac{1}{2}$) of a unit cell. Using EDS elemental mapping, we show that most Fe-rich exsolved particles correspond to La and Sr depletion (Fig. 1g). There is also variation observed in La and Sr signal, compared to the LSF film matrix, for regions which are depleted in Fe.

We observe four main categories of nanostructures formed *via* surface and bulk exsolution: (i) surface core–shell, (ii) bulk core–shell, (iii) adjacent particles, and (iv) independent particles (Fig. 2). We demonstrated in our recent paper using FFT analysis that the bulk exsolved particles are in fact metallic Fe, while the surface exsolved particles are Fe oxide (either Fe_3O_4 or γ-Fe_2O_3 [42]) due to exposure to air after exsolution.[42] We observe majority of nanostructures to be exsolved at interfaces in the LSF film indicating the activation energy of Fe nucleation is likely lower at the interfaces. The core–shell structures of surface and bulk particles, both exsolved at phase boundaries of perovskite matrix and RP phase, can be seen in STEM HAADF and BF images (Fig. 2a–f). STEM HAADF images display *Z*-contrast, with the image intensity being proportional to the mean atomic number Z^n (where $n \sim 1.7$).[60] STEM BF images, on the other hand, show phase and diffraction contrast.[61] To highlight the complementary information provided by both methods, the difference between perovskite matrix and RP phase domains is more apparent in STEM BF images (phase and diffraction contrast), while the STEM HAADF images display *Z*-contrast making it easier to differentiate between Fe-rich and Fe-depleted particles.

The core of the surface particle is rich in Fe, while the shell has primarily Fe and La signals suggesting presence of La/Fe based oxide, which is confirmed from quantitative analysis in the next section (Fig. 3b; see ESI Fig. S1–S3† for individual EDS elemental maps). Because the STEM data are two-dimensional projections of a three-dimensional object, it is ambiguous at times to distinguish the nanostructure from the surrounding matrix. Similarly, the bulk core–shell particle also has an Fe-rich core (Fig. 3d).

'Adjacent particles' are defined as nanostructures that are adjacent to each other after exsolution, with distinct high and low *Z* contrast in STEM HAADF imaging as well as phase/diffraction contrast in STEM BF imaging (Fig. 2h–i). These adjacent particles correspond to Fe-rich particles in the bulk resulting in Fe-depleted regions in the immediate vicinity (Fig. 3e–f). Such adjacent particles are observed throughout the LSF film after exsolution, and more examples can be seen in Fig. 4.

'Independent particles' are Fe-rich particles with no considerable Fe-depleted region nearby (Fig. 2j–l). These particles are also formed throughout the film *via* bulk exsolution (Fig. 4). These independent particles have a very thin shell

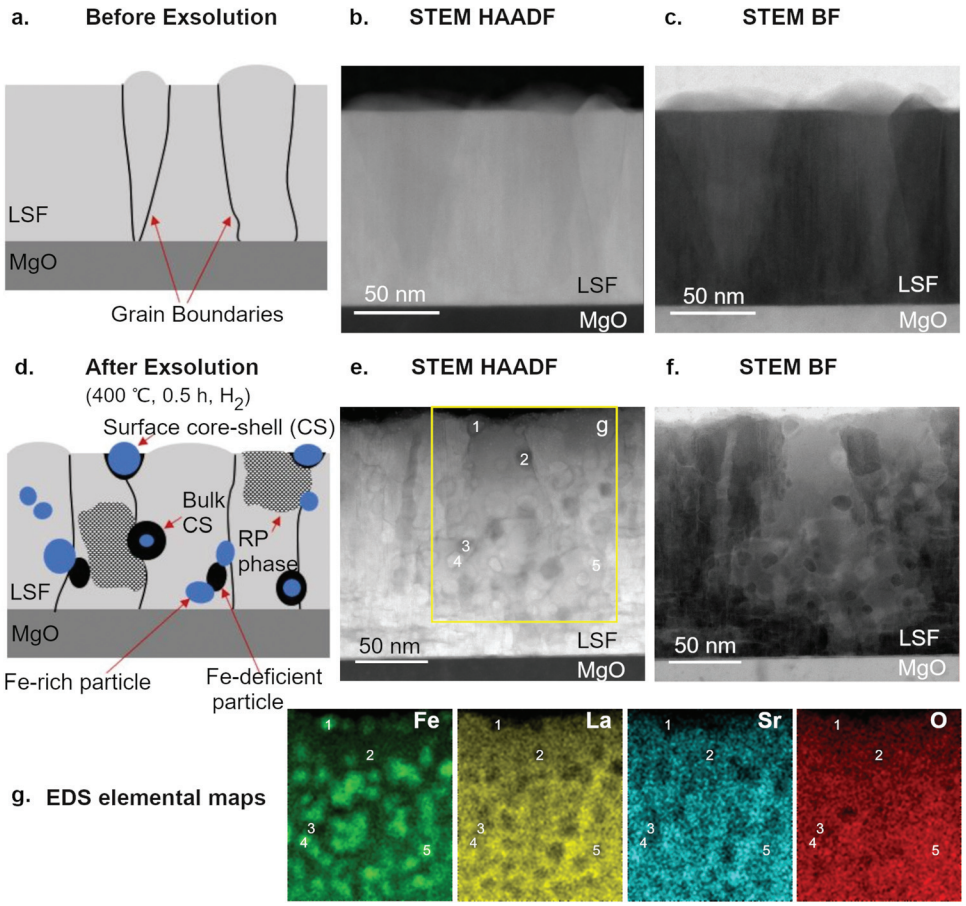

Fig. 1 $La_{0.6}Sr_{0.4}FeO_3$ (LSF) thin films were deposited by pulsed laser deposition (PLD) on 001-oriented MgO single crystals (a) and analyzed using scanning TEM (STEM) high-angle annular dark field (HAADF) images (b) and STEM bright-field (BF) images (c). Treatment of the films in 0.5 torr H_2 at 400 °C for 0.5 h induced Fe exsolution, yielding a variety of Fe-rich and Fe-depleted nanostructures and oxide phases through the film depth (d–f). EDS elemental maps (net counts) of Fe K, La L, Sr Ka and O K showing Fe exsolution throughout the LSF film (g).

(~1–2 nm) which appears dark in *Z*-contrast images (Fig. 4a), suggesting chemistry like the shell of bulk core–shell particles characterized earlier. However, we categorized these particles as independent because clearly the Fe-rich 'core' region comprises of majority of the particle, unlike the bulk core–shell particle where both core and shell are prominently observed.

Geometry of exsolved nanostructures in LSF

The Fe-rich nanostructures formed throughout the LSF film, both at surface and in bulk, are mostly observed to have ellipsoidal geometry. Most research studies to-date performed in H_2 (*e.g.* H_2/Ar) reducing environments, but focused only on surface exsolution, have also shown similar ellipsoidal or quasi-spherical geometry for exsolved particles.[16,36,62] Our results are thus consistent with the previous observations of surface particle geometry produced by H_2 environments, but we further demonstrate that the bulk exsolved particles also have similar ellipsoidal geometry. Neagu *et al.*[36] showed that the shape of the exsolved nanostructures can be tuned for various applications by changing the atmosphere for exsolution treatment as they explored with faceted particle growth in a vacuum environment. Our results show that both surface and bulk exsolved particles will likely maintain similar geometry depending on the exsolution treatment. For the exsolved particles in this study, the shape factor (ratio of major axis length to minor axis, a/b) was calculated to be 1.4 ± 0.4 using ~30 particles (see Fig. S4 in ESI†). On average, the size of Fe-rich nanostructures is 12.1 ± 4.8 nm (Fig. 5). We don't observe any significant variation in particle size with respect to the depth of the film.

The fact that the exsolved particles can be ellipsoidal points to the possibility of further designing this property through spatially orienting the particles. One might wish to orient the major axis of the ellipsoids to be parallel, perpendicular, or random, and this work would be foundational to developing such a future hypothesis. An example of functionality related to spatial orientation and vicinity of the produced nanostructures is electronic transport, wherein orienting the major axes of the particles in a parallel fashion could provide a more direct percolating pathway from particle-to-particle, thus enhancing conductivity through the particles. Alternatively, if the particles were designed for light absorption and/or scatter-

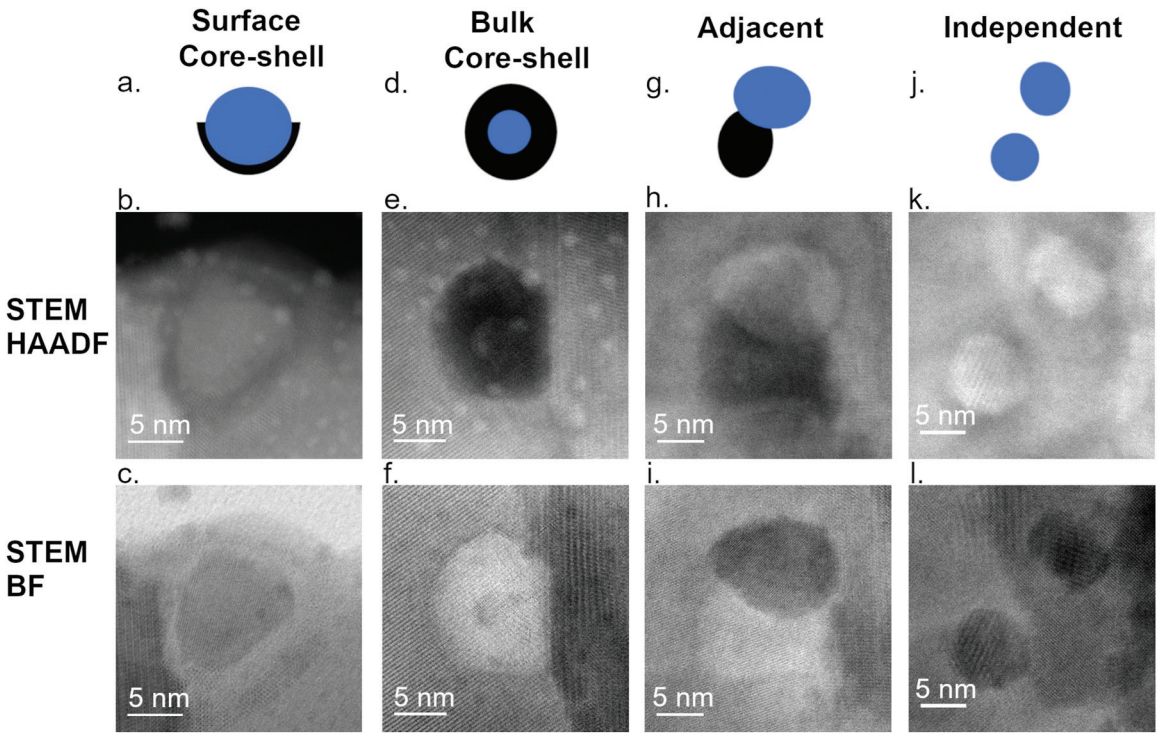

Fig. 2 Different types of Fe-based nanostructures observed in LSF thin film *via* exsolution shown using schematics, STEM HAADF images and STEM BF images. Surface core–shell (a–c) and bulk core–shell (d–f) structures have Fe-rich core and Fe-depleted shell. Another observed nanostructure is adjacent Fe-rich and Fe-depleted particles (g–i). Independent Fe-rich nanostructures (without adjacent Fe-depleted regions) are also observed throughout the LSF film (j–l).

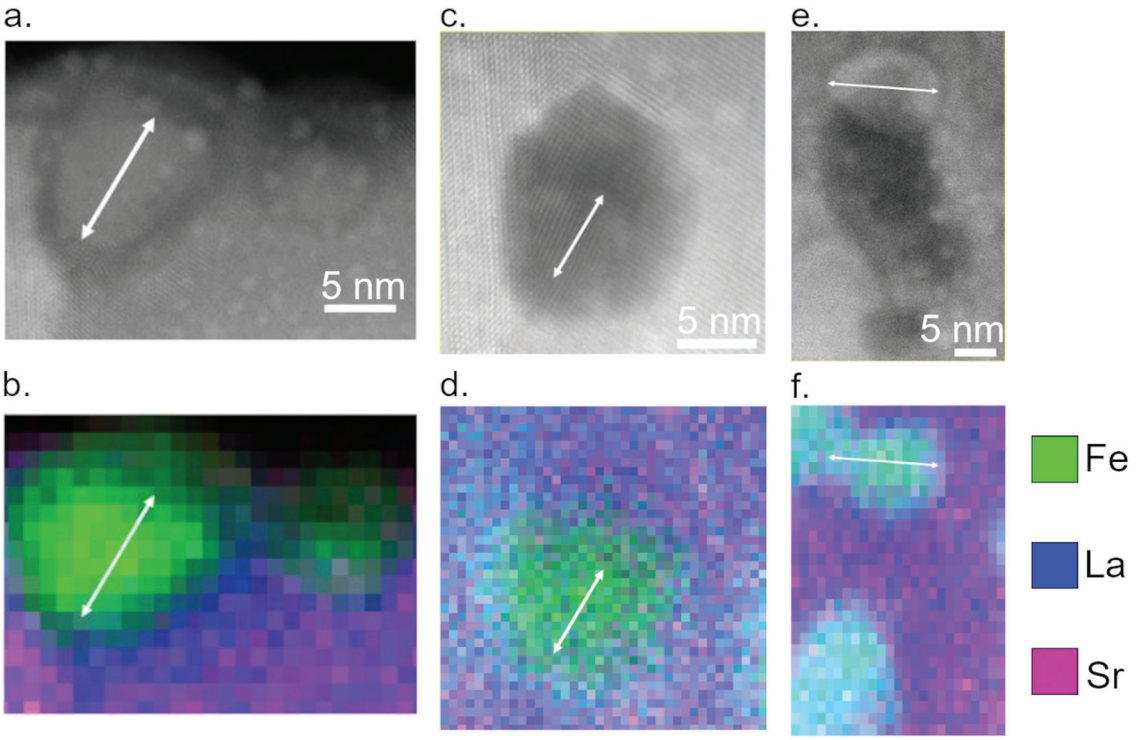

Fig. 3 STEM-HAADF images and overlay of EDS elemental maps (net counts) of surface core–shell particle (a and b), bulk core–shell (c and d) and adjacent particles (e and f).

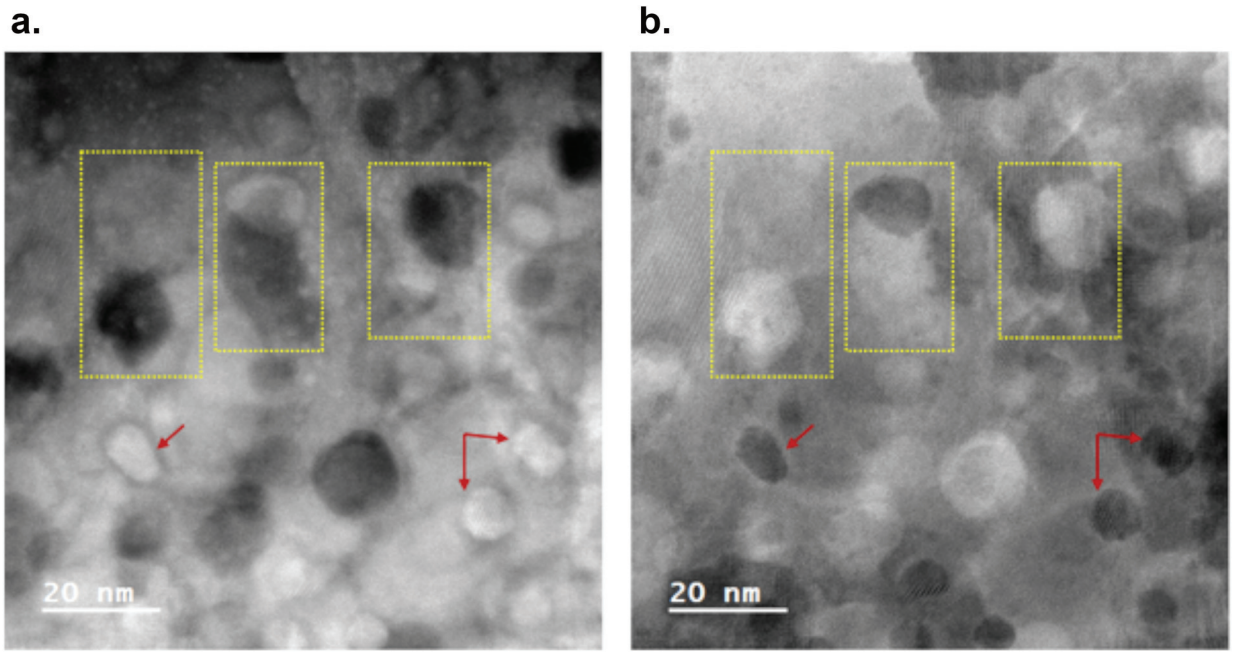

Fig. 4 STEM HAADF (a) and BF (b) images showing variety of 'adjacent' Fe-rich and Fe-depleted particles observed, some marked with yellow outline. 'Independent' Fe-rich particles are marked with red arrows.

ing, it could be beneficial to orient their major axis parallel to incident illumination for optimal photon coupling.

Quantitative analysis of bulk and surface nanostructures

The elemental compositional analysis for the various nanostructures demonstrates that the exsolution of Fe directly affects the nearby regions in the film. We observe two main phenomena with quantitative analysis: (a) formation of lanthanum ferrite or $La_xFe_yO_{3-\delta}$ (LFO) around Fe particles because of reaction with the LSF matrix, and (b) formation of Fe-depleted LSF adjacent to many Fe particles. Extracting the absolute composition of the various Fe-based nanostructures is challenging due to unavoidable contribution from the LSF matrix through the thickness of TEM lamellae specimen. However, useful results were obtained on the relative compositional changes between the exsolved nanostructures and the matrix. We quantified the concentration of cations using the Cliff–Lorimer method.[57–59]

The surface core–shell particle is rich in Fe and depleted in both La and Sr, compared to the LSF matrix (Fig. 6a). There is a decrease in HAADF intensity at the 'shell' region of the particle (points 1 and 4). Points 2 and 3 correspond to the particle core region, while point 5 corresponds to the LSF matrix. Point 2 corresponds to about 97 at% Fe, demonstrating that the core of the particle is Fe-based only.[42] The gradual increase of La content and negligible change in Sr content, from the core to shell region, indicate that the Fe core is surrounded by LFO. Considering the sum of all cation concentrations to be 100 at%, the LSF matrix (as prepared) correspond to 50 at% Fe, 30 at% La and 20 at% Sr. Here, the LSF matrix region is 36.5 at% Fe, 42.4 at% La and 21.1 at% Sr (Fig. 6a, point 5). This indicates that exsolution of the surface Fe particle resulted in depletion of Fe in the surrounding perovskite matrix.

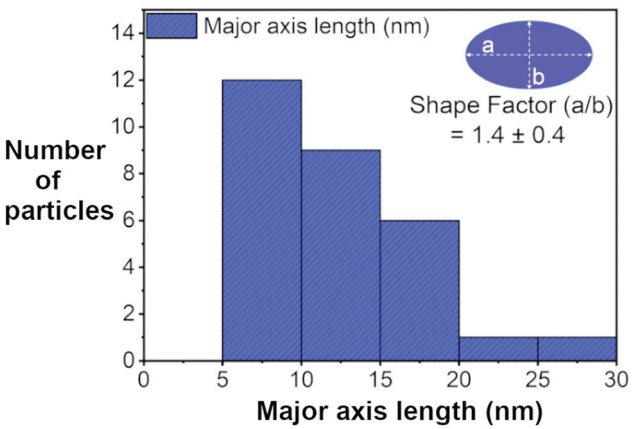

Fig. 5 Particle size distribution of Fe-rich nanostructures (based on major length 'a') formed throughout the LSF film *via* bulk exsolution.

Although the contribution of the LSF matrix is more prominent in the bulk core–shell particle, our analysis suggests that the core is Fe-rich and the shell is made of LFO like the surface particle, Fig. 6b. We observe local increase in HAADF intensity corresponding to the core of bulk core–shell particle (point1, Fig. 6b). Like the surface particle, the core is rich in Fe and depleted in La and Sr. The increasing concentration of La in the shell region (between points 2 and 3, Fig. 6b), while the Sr concentrations remains similar, indicates that the shell is made of LFO. This is like the observation made for the surface particle.

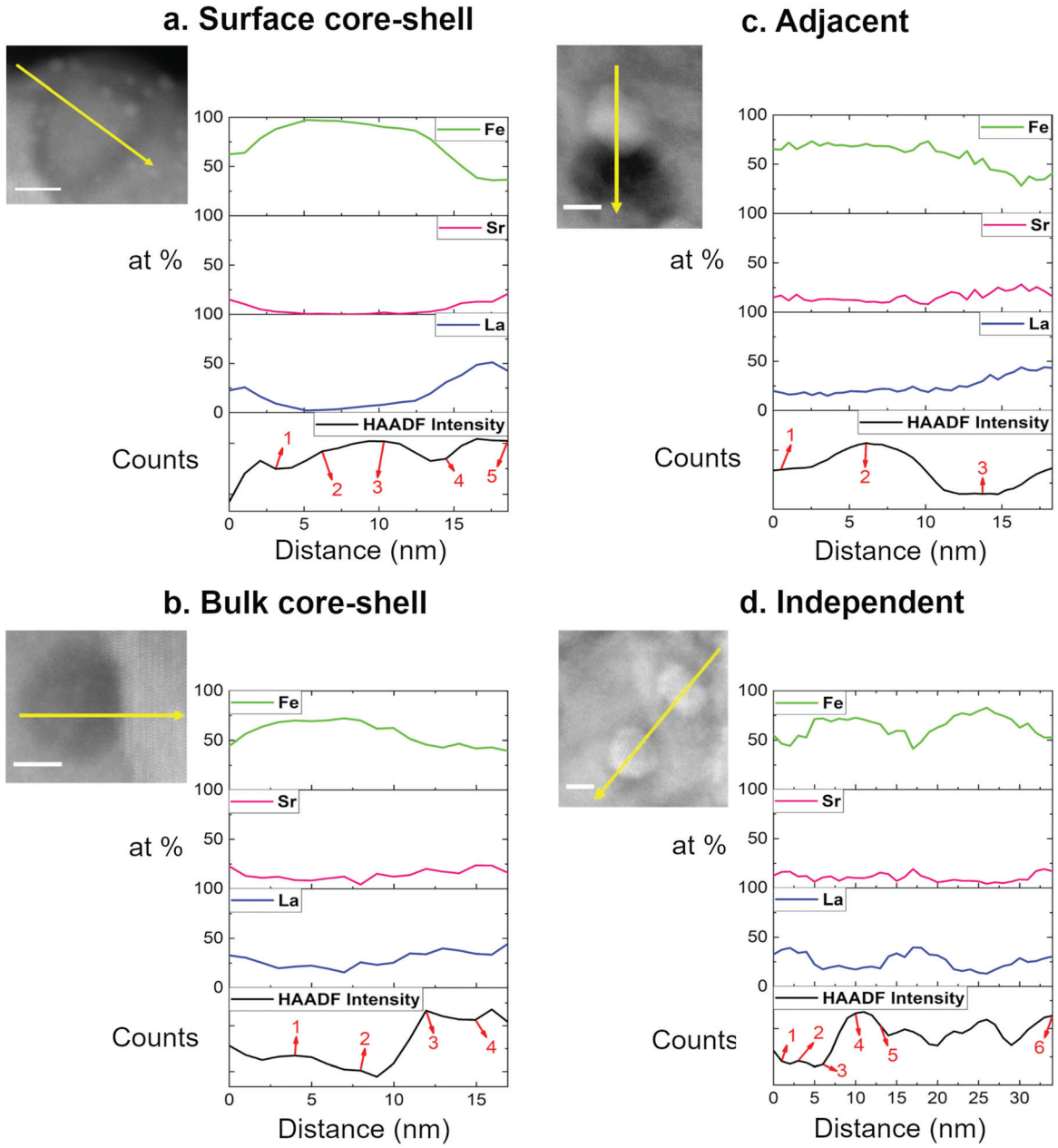

Fig. 6 STEM-HAADF images and line profiles showing HAADF image intensity (counts) and elemental concentration (at%) of cations Fe, La, and Sr across surface core–shell (a), bulk core–shell (b), adjacent (c), and independent particles (d). Scale bar in HAADF images is 5 nm.

The quantitative results from adjacent particles show that exsolution of Fe in the LSF film can result in Fe-depleted LSF in the immediate vicinity of the Fe particles, Fig. 6c. The increase in HAADF intensity (point 2, Fig. 6c) corresponds to the position of the Fe particle, while the decrease in HAADF intensity (point 3, Fig. 6c) corresponds to the Fe-depleted particle. Going from the bright to dark particle, the Fe concentration gradually decreases while La and Sr concentrations gradually increase. However, the increase in Sr concentration is less prominent than La. We don't observe an increase in Fe concentration at the onset of the bright particle (between points 1 and 2, Fig. 6c) due to contribution from another superpositioned Fe-exsolved particle; the particle is slightly out of focus in the HAADF image but within the interaction volume. Furthermore, consistent La and Sr concentrations along the bright particle suggests it is the contribution from LSF matrix.

The quantitative analysis of independent particles confirms our hypothesis in the previous section that the composition of these particles is like bulk core–shell particles, with a primarily Fe 'core' region and thin LFO 'shell' (Fig. 6d). The Fe core location corresponds to a local maximum in HAADF intensity (point 4, Fig. 6d), and a plateau in the Fe content profile (5 nm–15 nm). The relatively consistent La and Sr content

within the particle (between points 3 and 5, Fig. 6d) is attributed to the LSF matrix concentration within the interaction volume. The elemental concentrations in the LSF matrix region are 52.7 at% Fe, 30.4 at% La and 16.9 at% Sr (point 1, Fig. 6d). Like the observation of the bulk core–shell particle, the La content increases going from the core to shell region (point 3 to 2, Fig. 6d), whereas the Sr signal remains unchanged, showing the presence of LFO shell around the independent particles. This is also evident by the dark contrast around the Fe-rich particles in the HAADF image of Fig. 6d.

The dark HAADF contrast of the LFO shell formed around the Fe particles (Fig. 6) suggests lower mean Z compared to the LSF film matrix, but can also be due to structural distortion at phase boundaries affecting the HAADF signal. Mean Z for a compound can be calculated using different methods; we used the following to estimate mean Z values:[63]

$$Z = \sqrt{\sum_{i=1}^{n} a_i Z_i^2}$$

where, a_i is the atomic fraction and Z_i is the atomic number of the constituent elements. Mean Z for $LaFeO_3$ and LSF are calculated to be 28.7 and 26.1 respectively. Since $LaFeO_3$ has higher mean Z than LSF, the shell would have a higher HAADF signal than the matrix if it was composed of $LaFeO_3$, which is not the case here. Thus, we can assume that La : Fe ratio is not 1 : 1 in the shell. Based on our quantitative analysis of shell regions as well as mean Z calculations, we believe the shell around the Fe particles to be a La-depleted and Fe-rich (perovskite-like) oxide, compared to the LSF matrix. The core–shell nature of some nanostructures could, for example, be leveraged in a situation where one wishes to tune a film's magnetic properties. In this case a variable to optimize is the thickness of the oxide shell and thus the volumetric ratio of metal core to metal oxide shell.

Formation of Ruddlesden–Popper phase (LSF_{214}) *via* bulk exsolution

STEM characterization and FFT analysis confirm that Fe exsolution in the LSF film creates local A-site rich domains of RP phase. The general formula of RP phase can be given by $A_{n+1}B_nO_{3n+1}$; *i.e.* A_2BO_4 for n = 1.[64] We found an inhomogeneous distribution of RP phases throughout the LSF film. XRD results, detailed elsewhere,[42] showed that perovskite LSF continues to be the dominant phase after exsolution with chemical expansion in the LSF lattice due to formation of oxygen vacancies. Many Fe nanostructures are observed to form at the boundaries of the LSF perovskite matrix and RP phases. Fig. 7a shows a bulk core–shell particle formed at the phase boundary between the original perovskite matrix (LSF_{113}) and RP phase (LSF_{214}) (Fig. 7).

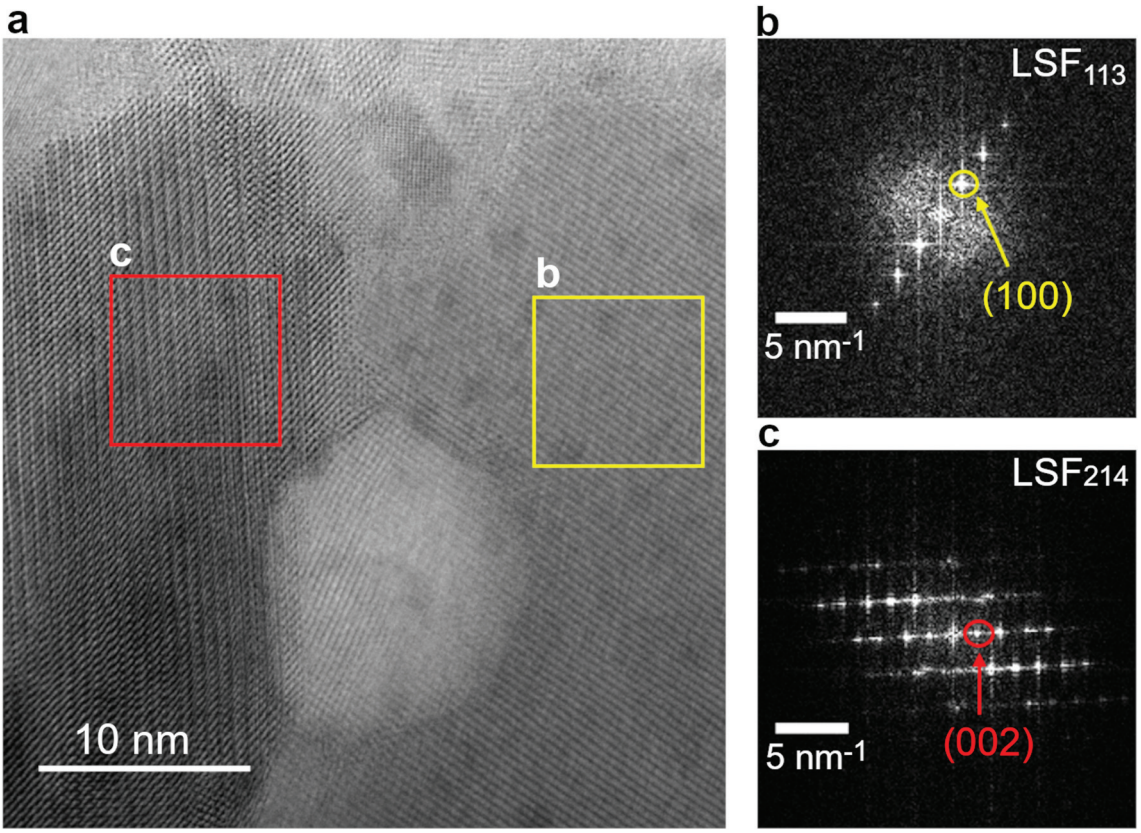

Fig. 7 STEM-BF image (a) and FFT patterns of LSF_{113} and LSF_{214} respectively (b and c).

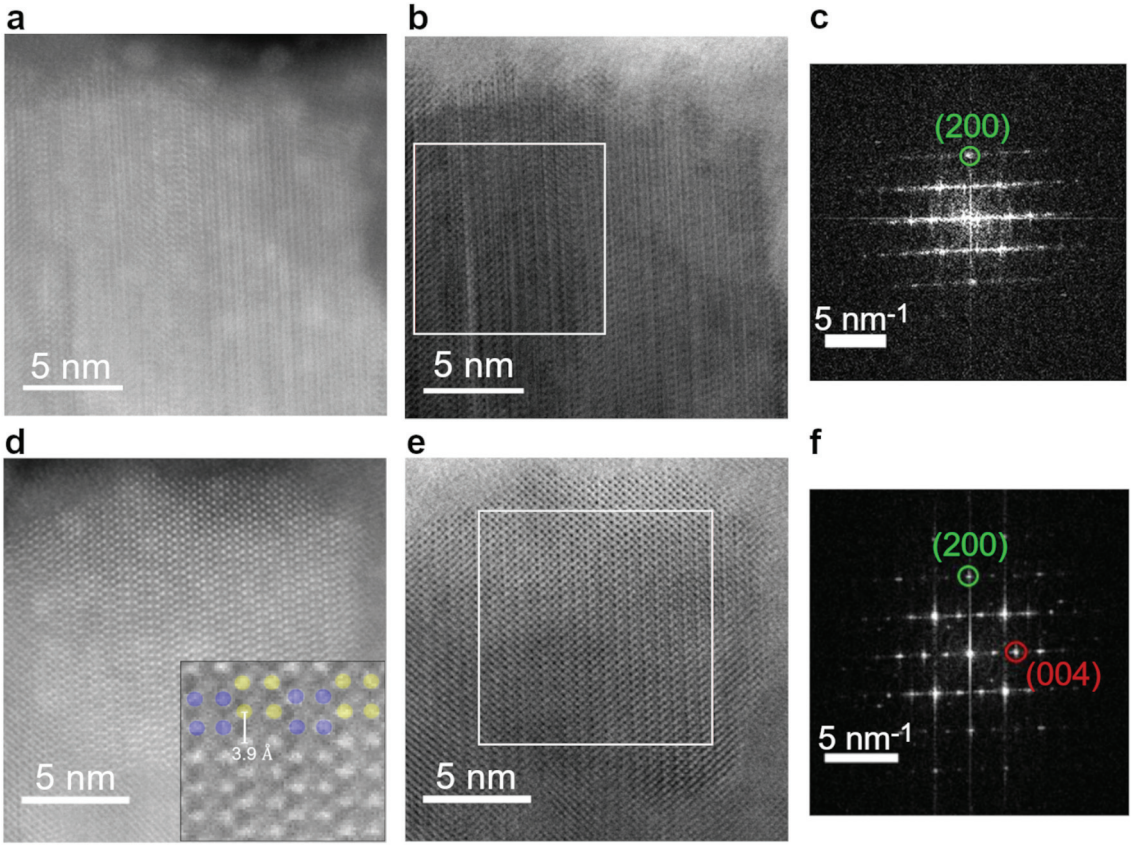

Fig. 8 Observation of two different stages of the RP phase formation *via* exsolution process shown with STEM HAADF images (a and d) and STEM BF images (b and e). Corresponding FFT patterns (c and f) are also shown. The yellow and purple circles in d highlight the shift of atomic columns in the fully transformed RP phase.

In the same specimen, we observe different stages of RP phase formation near the surface of the LSF film (Fig. 8). For the partially transformed phase (Fig. 8a and b), (200) planes with non-uniform linear contrast appear to be connected by zig-zag patterns, which is attributed to disordered planar defects.[65] These planar-like defects are manifested as horizontal streaking on the FFT pattern (Fig. 8c). In the fully transformed RP phase (Fig. 8d and e), we see well-ordered arrangement of planar defects, shifted by $\frac{1}{2}$a[100] as can be seen clearly in the inset of the HAADF image (Fig. 8d). Such ordered planar defects are commonly observed in A-site rich oxides, and have been discussed previously by Suzuki *et al.*[65] This results in sharp FFT spots, along with superlattice spots, as shown in Fig. 8f.

RP phase formation (simultaneous to Fe-exsolution) was also observed in a model epitaxial thin-film LSF (~20 nm) [see details in ESI, Fig. S5†]. The characterization of surface exsolution for this thin-film LSF has been previously published.[6] Our results on both the thick LSF film (~165 nm) and thin LSF film (~20 nm) confirm that with modifications in exsolution treatments, the formation of RP phase can be controlled to optimize exsolution of catalytic particles and thus achieve improved catalytic efficiency.

Conclusions

We report four distinct types of Fe-based nanostructures formed in LSF thin films (on MgO substrate) *via* bulk and surface exsolution: surface core–shell, bulk core–shell, adjacent and independent nanostructures. The core–shell particles are determined to have a metallic Fe core and LFO shell. The adjacent nanostructures are Fe exsolved particles with Fe-depleted LSF in their immediate vicinity. The independent nanostructures are found to have the same structure and chemistry like the bulk core–shell particles, but with a prominent Fe core region and very thin ~1–2 nm LFO shell. The exsolved bulk and surface particles have a shape factor of 1.4. We show that Fe exsolution creates local A-site rich domains of RP phase and two different stages of this phase formation *via* exsolution process is captured and analyzed using STEM imaging in this work. The phase boundaries, such as between RP phase and perovskite matrix, are attributed to be the primary sites for surface and bulk exsolution, suggesting the activation energy of Fe nucleation is lower at these boundaries. This work presents an in-depth nanostructure-based analysis of bulk and surface exsolution in thin films, offering a beneficial guide for scientists and engineers interested in explor-

ing exsolution to optimize advanced materials. In the future it would be valuable to systematically investigate the impact of film synthesis and processing conditions on the amount of each nanostructure type, to establish more predictive synthesis protocols for each type of nanostructure. This should point the way forward towards designing and realizing tunable functional materials containing a specific subset of the nanostructures presented here.

Author contributions

WJB and KS designed the study. JW prepared the thin films. KS conducted the STEM characterization and data analysis. KS wrote the manuscript and all authors contributed to editing/revision. WJB supervised the project.

Conflicts of interest

There are no conflicts to declare.

Acknowledgements

KS acknowledges support from US Department of Education Graduate Assistance in Areas of National Need (GAANN) Fellowship. WJB acknowledges support from the UCI new faculty start-up funding. For STEM-EDS characterization, the authors acknowledge the use of facilities and instrumentation at the UC Irvine Materials Research Institute (IMRI), which is supported in part by the National Science Foundation through the UC Irvine Materials Research Science and Engineering Center (MRSEC DMR-2011967). J. W. and B. Y. would like to thank the Exelon Corporation and the MIT Energy Initiative Seed Fund Program for supporting the work presented in this paper.

References

1 Y. Nishihata, *et al.* Self-regeneration of a Pd-perovskite catalyst for automotive emissions control, *Nature*, 2002, **418**, 164–167.
2 Y. Li, *et al.*, Controlling cation segregation in perovskite-based electrodes for high electro-catalytic activity and durability, *Chem. Soc. Rev.*, 2017, **46**, 6345–6378.
3 D. Neagu, G. Tsekouras, D. N. Miller, H. Ménard and J. T. S. Irvine, In situ growth of nanoparticles through control of non-stoichiometry, *Nat. Chem.*, 2013, **5**, 916–923.
4 J. Myung, D. Neagu, D. N. Miller and J. T. S. Irvine, Switching on electrocatalytic activity in solid oxide cells, *Nature*, 2016, **537**, 528.
5 T. Zhu, H. E. Troiani, L. V. Mogni, M. Han and S. A. Barnett, Ni-Substituted Sr(Ti,Fe)O3 SOFC Anodes: Achieving High Performance via Metal Alloy Nanoparticle Exsolution, *Joule*, 2018, **2**, 478–496.
6 J. Wang, *et al.*, Tuning Point Defects by Elastic Strain Modulates Nanoparticle Exsolution on Perovskite Oxides, *Chem. Mater.*, 2021, **33**, 5021–5034.
7 B. A. Rosen, Progress and Opportunities for Exsolution in Electrochemistry, *Electrochemistry*, 2020, **1**, 32–43.
8 K. Takehira, Highly Dispersed and Stable Supported Metal Catalysts Prepared by Solid Phase Crystallization Method, *Catal. Surv. Asia*, 2002, **6**, 19–32.
9 H. Tanaka, *et al.*, Self-Regenerating Rh- and Pt-Based Perovskite Catalysts for Automotive-Emissions Control, *Angew. Chem., Int. Ed.*, 2006, **45**, 5998–6002.
10 H. Tanaka, *et al.*, The intelligent catalyst having the self-regenerative function of Pd, Rh and Pt for automotive emissions control, *Catal. Today*, 2006, **117**, 321–328.
11 I. Tan, *et al.*, The Self-Regenerative 'Intelligent' Catalyst for Automotive Emissions Control, *Key Eng. Mater.*, 2006, **317–318**, 833–836.
12 M. Taniguchi, *et al.*, The self-regenerative Pd-, Rh-, and Pt-perovskite catalysts, *Top. Catal.*, 2007, **42**, 367–371.
13 G. Tsekouras, D. Neagu and J. T. S. Irvine, Step-change in high temperature steam electrolysis performance of perovskite oxide cathodes with exsolution of B-site dopants, *Energy Environ. Sci.*, 2012, **6**, 256–266.
14 C. Arrivé, T. Delahaye, O. Joubert and G. Gauthier, Exsolution of nickel nanoparticles at the surface of a conducting titanate as potential hydrogen electrode material for solid oxide electrochemical cells, *J. Power Sources*, 2013, **223**, 341–348.
15 B. H. Park and G. M. Choi, Ex-solution of Ni nanoparticles in a La0.2Sr0.8Ti1−xNixO3−δ alternative anode for solid oxide fuel cell, *Solid State Ionics*, 2014, **262**, 345–348.
16 D. Neagu, *et al.*, Nano-socketed nickel particles with enhanced coking resistance grown *in situ* by redox exsolution, *Nat. Commun.*, 2015, **6**, 8120.
17 S. Liu, Q. Liu and J.-L. Luo, Highly Stable and Efficient Catalyst with In Situ Exsolved Fe–Ni Alloy Nanospheres Socketed on an Oxygen Deficient Perovskite for Direct CO_2 Electrolysis, *ACS Catal.*, 2016, **6**, 6219–6228.
18 Y. Gao, D. Chen, M. Saccoccio, Z. Lu and F. Ciucci, From material design to mechanism study: Nanoscale Ni exsolution on a highly active A-site deficient anode material for solid oxide fuel cells, *Nano Energy*, 2016, **27**, 499–508.
19 Y. Zhu, *et al.*, Promotion of Oxygen Reduction by Exsolved Silver Nanoparticles on a Perovskite Scaffold for Low-Temperature Solid Oxide Fuel Cells, *Nano Lett.*, 2016, **16**, 512–518.
20 B. D. Madsen, W. Kobsiriphat, Y. Wang, L. D. Marks and S. A. Barnett, Nucleation of nanometer-scale electrocatalyst particles in solid oxide fuel cell anodes, *J. Power Sources*, 2007, **166**, 64–67.
21 W. Kobsiriphat, B. D. Madsen, Y. Wang, L. D. Marks and S. A. Barnett, La0.8Sr0.2Cr1−xRuxO3−δ–Gd0.1Ce0.9O1.95 solid oxide fuel cell anodes: Ru precipitation and electrochemical performance, *Solid State Ionics*, 2009, **180**, 257–264.

22 W. Kobsiriphat, *et al.*, Nickel- and Ruthenium-Doped Lanthanum Chromite Anodes: Effects of Nanoscale Metal Precipitation on Solid Oxide Fuel Cell Performance, *J. Electrochem. Soc.*, 2010, **157**, B279–B284.
23 D. M. Bierschenk, *et al.*, Pd-substituted (La,Sr)CrO3−δ–Ce0.9Gd0.1O2−δ solid oxide fuel cell anodes exhibiting regenerative behavior, *J. Power Sources*, 2011, **196**, 3089–3094.
24 L. Adijanto, V. B. Padmanabhan, R. Küngas, R. J. Gorte and J. M. Vohs, Transition, metal-doped rare earth vanadates: a regenerable catalytic material for SOFC anodes, *J. Mater. Chem.*, 2012, **22**, 11396–11402.
25 D. Neagu, *et al.*, Demonstration of chemistry at a point through restructuring and catalytic activation at anchored nanoparticles, *Nat. Commun.*, 2017, **8**, 1–8.
26 S. Sengodan, *et al.*, Self-Decorated MnO Nanoparticles on Double Perovskite Solid Oxide Fuel Cell Anode by in Situ Exsolution, *ACS Sustainable Chem. Eng.*, 2017, **5**, 9207–9213.
27 V. Kyriakou, *et al.*, Co-electrolysis of H_2O and CO_2 on exsolved Ni nanoparticles for efficient syngas generation at controllable H2/CO ratios, *Appl. Catal., B*, 2019, **258**, 117950.
28 C. Zhu, *et al.*, Electrochemical conversion of methane to ethylene in a solid oxide electrolyzer, *Nat. Commun.*, 2019, **10**, 1–8.
29 N. Hou, *et al.*, A-Site Ordered Double Perovskite with in Situ Exsolved Core–Shell Nanoparticles as Anode for Solid Oxide Fuel Cells, *ACS Appl. Mater. Interfaces*, 2019, **11**, 6995–7005.
30 R. Thalinger, *et al.*, Ni–perovskite interaction and its structural and catalytic consequences in methane steam reforming and methanation reactions, *J. Catal.*, 2016, **337**, 26–35.
31 S. Singh, *et al.*, Role of 2D and 3D defects on the reduction of LaNiO3 nanoparticles for catalysis, *Sci. Rep.*, 2017, **7**, 10080.
32 D. Hosseini, *et al.*, Reversible Exsolution of Dopant Improves the Performance of Ca2Fe2O5 for Chemical Looping Hydrogen Production, *ACS Appl. Mater. Interfaces*, 2019, **11**, 18276–18284.
33 G. Dimitrakopoulos, A. F. Ghoniem and B. Yildiz, *In situ* catalyst exsolution on perovskite oxides for the production of CO and synthesis gas in ceramic membrane reactors, *Sustainable Energy Fuels*, 2019, **3**, 2347–2355.
34 K. Kousi, D. Neagu, L. Bekris, E. Papaioannou and I. S. Metcalfe, Endogenous Nanoparticles Strain Perovskite Host Lattice Providing Oxygen Capacity and Driving Oxygen Exchange and CH4 Conversion to Syngas, *Angew. Chem., Int. Ed.*, 2020, **59**, 2510.
35 Y. Zhu, *et al.*, Synergistically enhanced hydrogen evolution electrocatalysis by in situ exsolution of metallic nanoparticles on perovskites, *J. Mater. Chem. A*, 2018, **6**, 13582–13587.
36 D. Neagu, *et al.*, *In Situ* Observation of Nanoparticle Exsolution from Perovskite Oxides: From Atomic Scale Mechanistic Insight to Nanostructure Tailoring, *ACS Nano*, 2019, **13**, 12996–13005.
37 H. Han, *et al.*, Lattice strain-enhanced exsolution of nanoparticles in thin films, *Nat. Commun.*, 2019, **10**, 1471.
38 Y. Chen, *et al.*, Exceptionally active iridium evolved from a pseudo-cubic perovskite for oxygen evolution in acid, *Nat. Commun.*, 2019, **10**, 1–10.
39 B. Yan, *et al.*, Highly active subnanometer Rh clusters derived from Rh-doped SrTiO3 for CO_2 reduction, *Appl. Catal., B*, 2018, **237**, 1003–1011.
40 H. Lv, *et al.*, In situ exsolved FeNi3 nanoparticles on nickel doped Sr2Fe1.5Mo0.5O6−δ perovskite for efficient electrochemical CO_2 reduction reaction, *J. Mater. Chem. A*, 2019, **7**, 11967–11975.
41 Y.-F. Sun, *et al.*, Toward a rational photocatalyst design: a new formation strategy of co-catalyst/semiconductor heterostructures via in situ exsolution, *Chem. Commun.*, 2018, **54**, 1505–1508.
42 J. Wang, *et al.*, Exsolution Synthesis of Nanocomposite Perovskites with Tunable Electrical and Magnetic Properties, *Adv. Funct. Mater.*, 2021, 2108005.
43 O. Kwon, *et al.*, Exsolution trends and co-segregation aspects of self-grown catalyst nanoparticles in perovskites, *Nat. Commun.*, 2017, **8**, 15967.
44 T. Götsch, *et al.*, Structural investigations of La0.6Sr0.4FeO3−δ under reducing conditions: kinetic and thermodynamic limitations for phase transformations and iron exsolution phenomena, *RSC Adv.*, 2018, **8**, 3120–3131.
45 R. Thalinger, M. Gocyla, M. Heggen, B. Klötzer and S. Penner, Exsolution of Fe and SrO Nanorods and Nanoparticles from Lanthanum Strontium Ferrite La0.6Sr0.4FeO3−δ Materials by Hydrogen Reduction, *J. Phys. Chem. C*, 2015, **119**, 22050–22056.
46 Y.-R. Jo, *et al.*, Growth Kinetics of Individual Co Particles Ex-solved on $SrTi_{0.75}Co_{0.25}O_{3-\delta}$ Polycrystalline Perovskite Thin Films, *J. Am. Chem. Soc.*, 2019, **141**, 6690–6697.
47 S. Joo, *et al.*, Cation-swapped homogeneous nanoparticles in perovskite oxides for high power density, *Nat. Commun.*, 2019, **10**, 1–9.
48 T.-S. Oh, *et al.*, Evidence and Model for Strain-Driven Release of Metal Nanocatalysts from Perovskites during Exsolution, *J. Phys. Chem. Lett.*, 2015, **6**, 5106–5110.
49 Y. Gao, *et al.*, Energetics of Nanoparticle Exsolution from Perovskite Oxides, *J. Phys. Chem. Lett.*, 2018, **9**, 3772–3778.
50 K. J. Kim, *et al.*, Facet-Dependent *in Situ* Growth of Nanoparticles in Epitaxial Thin Films: The Role of Interfacial Energy, *J. Am. Chem. Soc.*, 2019, **141**, 7509–7517.
51 D. Zubenko, S. Singh and B. A. Rosen, Exsolution of Re-alloy catalysts with enhanced stability for methane dry reforming, *Appl. Catal., B*, 2017, **209**, 711–719.
52 M. B. Katz, *et al.*, Reversible precipitation/dissolution of precious-metal clusters in perovskite-based catalyst materials: Bulk versus surface re-dispersion, *J. Catal.*, 2012, **293**, 145–148.
53 S. Dai, S. Zhang, M. B. Katz, G. W. Graham and X. Pan, *In Situ*Observation of Rh-$CaTiO_3$ Catalysts during Reduction

and Oxidation Treatments by Transmission Electron Microscopy, *ACS Catal*, 2017, **7**, 1579–1582.

54 I.-T. Chiu, *et al.*, Cation and anion topotactic transformations in cobaltite thin films leading to Ruddlesden-Popper phases, *Phys. Rev. Mater.*, 2021, **5**, 064416.

55 J. Li, *et al.*, Topotactic phase transformations by concerted dual-ion migration of B-site cation and oxygen in multivalent cobaltite La–Sr–Co–Ox films, *Nano Energy*, 2020, **78**, 105215.

56 K. Kousi, D. Neagu, L. Bekris, E. I. Papaioannou and I. S. Metcalfe, Endogenous Nanoparticles Strain Perovskite Host Lattice Providing Oxygen Capacity and Driving Oxygen Exchange and CH4 Conversion to Syngas, *Angew. Chem.*, 2020, **132**, 2531–2540.

57 G. Cliff and G. W. Lorimer, The quantitative analysis of thin specimens, *J. Microsc.*, 1975, **103**, 203–207.

58 G. W. Lorimer, Quantitative X-ray microanalysis of thin specimens in the transmission electron microscope; a review, *Mineral. Mag.*, 1987, **51**, 49–60.

59 W. J. Bowman, A. Darbal and P. A. Crozier, Linking Macroscopic and Nanoscopic Ionic Conductivity: A Semiempirical Framework for Characterizing Grain Boundary Conductivity in Polycrystalline Ceramics, *ACS Appl. Mater. Interfaces*, 2020, **12**, 507–517.

60 K. Sohlberg, T. J. Pennycook, W. Zhou and S. J. Pennycook, Insights, into the physical chemistry of materials from advances in HAADF-STEM, *Phys. Chem. Chem. Phys.*, 2015, **17**, 3982–4006.

61 S. J. Pennycook, Z-contrast stem for materials science, *Ultramicroscopy*, 1989, **30**, 58–69.

62 S. Yu, *et al.*, Metal Nanoparticle Exsolution on a Perovskite Stannate Support with High Electrical Conductivity, *Nano Lett.*, 2020, **20**, 3538–3544.

63 P. G. T. Howell, K. M. W. Davy and A. Boyde, Mean atomic number and backscattered electron coefficient calculations for some materials with low mean atomic number, *Scanning*, 1998, **20**, 35–40.

64 S. N. Ruddlesden and P. Popper, The compound Sr3Ti2O7 and its structure, *Acta Crystallogr.*, 1958, **11**, 54–55.

65 T. Suzuki, Y. Nishi and M. Fujimoto, Defect structure in homoepitaxial non-stoichiometric strontium titanate thin films, *Philos. Mag. A*, 2000, **80**, 621–637.

Electronic Supplementary Material (ESI) for Nanoscale.

SUPPLEMENTARY INFORMATION

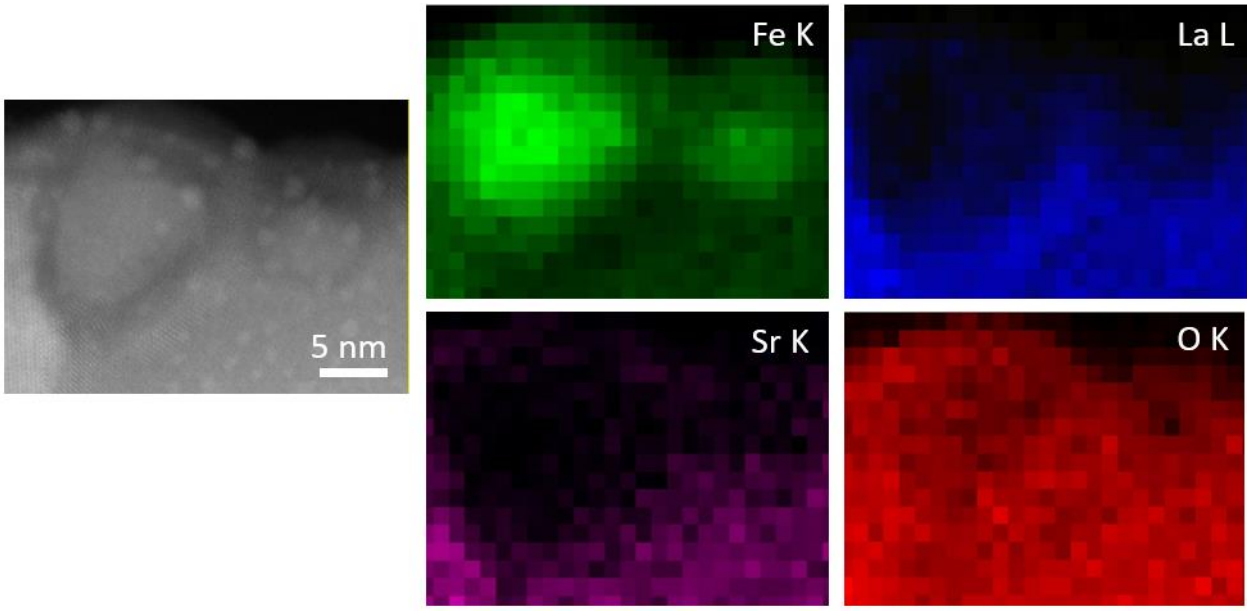

Fig. S1: STEM HAADF image of surface core-shell nanostructure and corresponding elemental EDS maps of Fe K, La L, Sr K and O K.

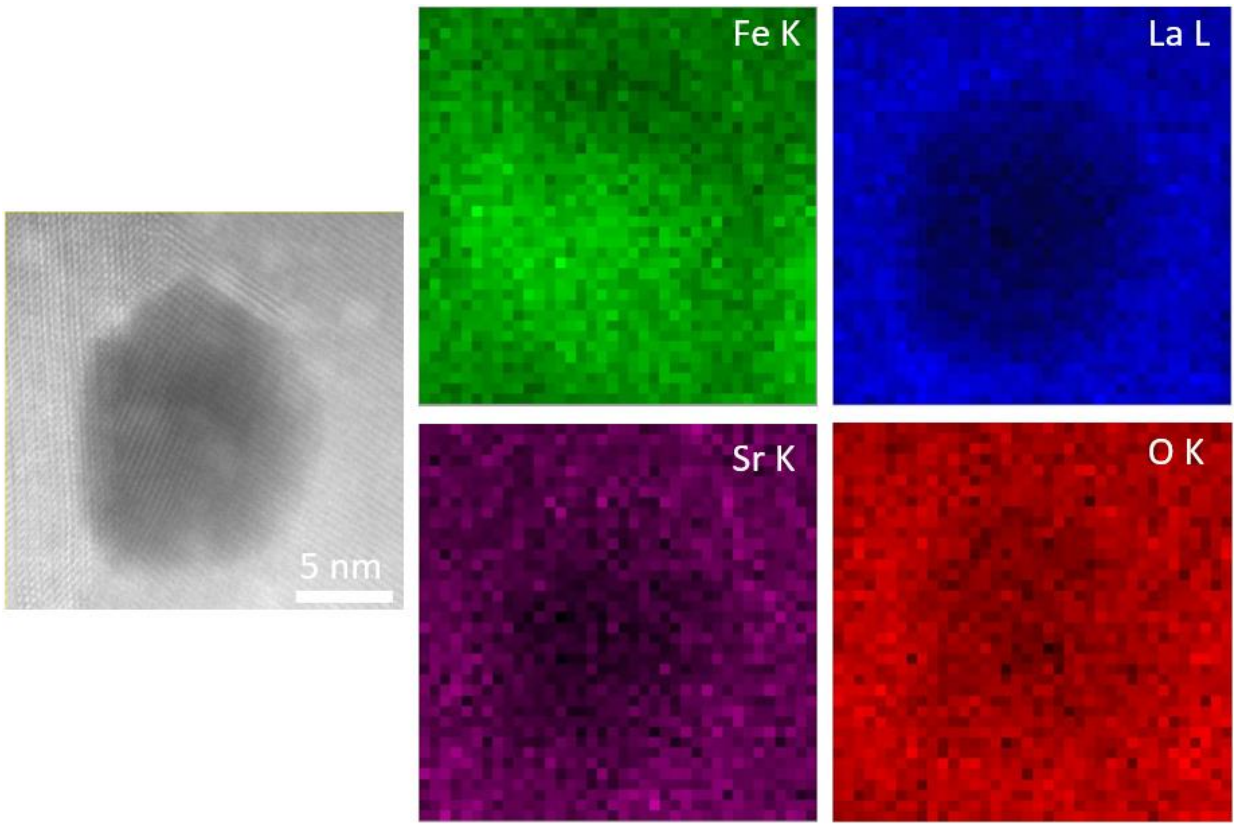

Fig. S2: STEM HAADF image of bulk core-shell nanostructure and corresponding elemental EDS maps of Fe K, La L, Sr K and O K.

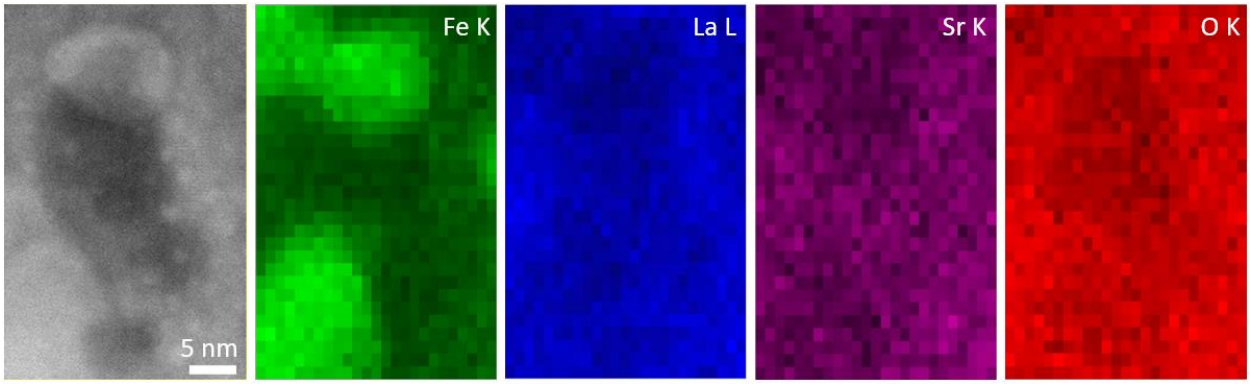

Fig. S3: STEM HAADF image of adjacent Fe-rich and Fe-depleted nanostructures and corresponding elemental EDS maps of Fe K, La L, Sr K and O K.

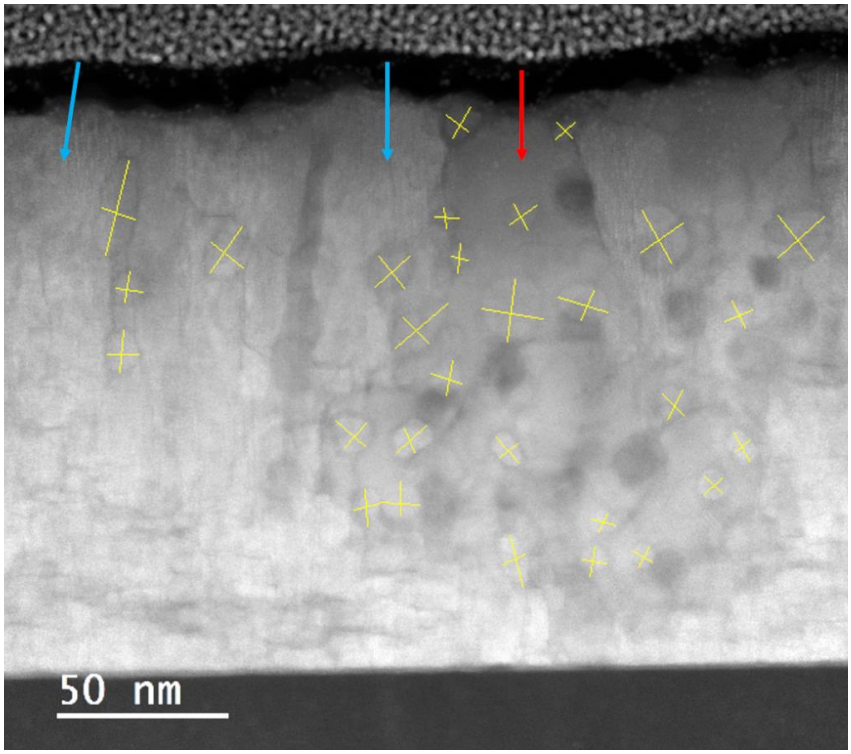

Fig. S4: STEM HAADF image showing markings for major axis 'a' and minor axis 'b' dimensions of the ellipsoidal particles in LSF exsolved film used for calculations of average size of Fe nanostructures and shape factor. Blue arrows mark some of the LSF_{214} (RP) domains. Red arrows mark the LSF_{113} matrix region.

Fe exsolution mechanism was studied in a model single-crystal LSF thin film:

A model thin film of LSF, ~20 nm, was grown epitaxially on Nb-doped STO to investigate atomic-scale properties of exsolved thin films to complement observations of relatively 'thick' LSF films (~165 nm). The thin film of LSF/Nb:STO was reduced at 650 ^{o}C in 3% H_2/N_2. More details of the thin film deposition can be found elsewhere[6].The STEM EDS and EELS data of the model LSF thin film is obtained with a probe-corrected STEM operating at 200 kV (JEOL Grand ARM 200F at Harvard University equipped with a Gatan Enfinium energy-loss spectrometer capable of dual EELS). The EELS data presented and used for analysis here were acquired using a 2D spectrum image, and represent the sum of ~ 35 spectra each acquired with an acquisition time of 0.01 s. The EEL spectrometer entrance aperture diameter was 5 mm, and the dispersion was 1 eV. EEL spectra were calibrated by aligning the La M_5 peak (830 eV), and background subtraction was performed by extrapolation of the inverse power law function fitted to the Fe L_{23} and La M_{45} pre-edge signals. After background subtraction, the intensity of the Fe and La core-loss signals were calculated via integration within the signal integration windows provided in table 1. The zero-loss peak was recorded at each pixel position in the spectrum image, and the specimen thickness was ~ 0.15 inelastic mean free paths.

Table S1: Parameters used for EELS data fitting

	Fe L_{23}	La M_{45}
Background fitting window (eV)	617 – 684	748 – 815
Signal integration window (eV)	748 – 815	816– 866

RP mosaic structures [64,65] containing Fe-depleted planar defects were observed following Fe exsolution from a model epitaxial LSF thin film. The defect structures, so-called RP mosaics (Fig. S5), have been detailed previously by Suzuki *et al.* [64] and observed again by Brooks *et al.* [65] while studying A-site-excess $SrTiO_3$. Following thermochemical exsolution treatment, Fe oxide particles were observed partially submerged in the surface of the LSF thin film, shown elsewhere[6].

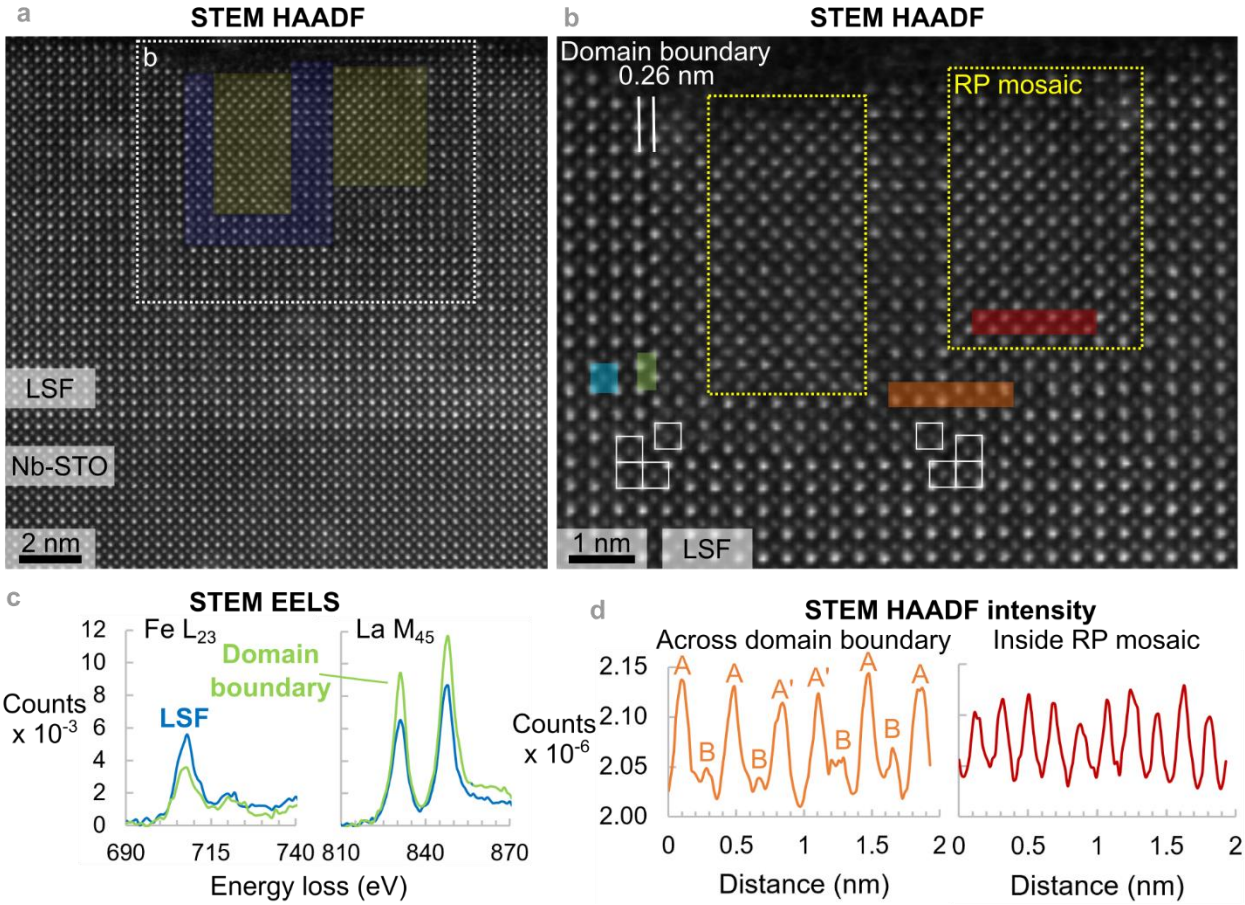

Fig. S5: Atomic-scale characterization of RP domains. (a) STEM HAADF image of Ruddleson-Popper domains in LSF (type 1 domain highlighted in blue and RP mosaics in yellow). (b) Expanded view of the RP domain boundary showing A-site terminations (type-1 domain corners are indicated by white squares). RP mosaic regions show overlap between displaced domains and LSF matrix. (c) Core-loss EELS of Fe L_{23} and La M_{45} acquired from the LSF matrix (blue) and the domain boundary (green) regions highlighted blue and green in (b), respectively. The background subtracted signals were acquired from two regions of (0.246 nm)^2. (d) STEM HAADF intensity profiles from a domain boundary and from inside a RP mosaic; profiles were calculated in the regions highlighted orange and red, respectively. Unlike at the domain boundary, atomic number (Z) contrast between A- and B- sites is not visible in the RP mosaic.

Atomic resolution STEM imaging and EELS analysis suggest that Fe may be diffusing along {001} planes during exsolution, causing Fe deficiency in these planes and the formation of RP

mosaic structures. Similar to the description provided by Suzuki *et al.*, we observed two types of embedded domains. The first type has the perovskite structure but is displaced relative to the LSF matrix by ½a[110] (blue region in Fig. S5a). Between the LSF and type-1 domain there is a domain boundary along {001} planes. The domain boundary consists of two A-site terminations (Fig. S5b) with a (001) interplanar spacing of 0.26 nm +/- 0.02 nm, reduced from 0.36 +/- 0.02 nm in the LSF (uncertainty is width of one pixel; Fig. S5b). The A-A domain boundary is evident in the integrated HAADF intensity profile (Fig. S5d) calculated in the orange region of Fig. S5b. The second domain type also has the symmetry of the LSF perovskite matrix (yellow regions in Fig. S5a, and boxed regions of Fig. S5b). However, the HAADF intensity at the A- and B-sites is nearly equal (Fig. S5d), indicating that the mean atomic number in each atomic column is approximately equal. Thus, the HAADF image of these RP mosaics (Fig. S5b) is thought to be a projection of type-1 domains overlapping with the LSF matrix.

The 0.26 nm A-A domain boundary was Fe-depleted relative to the LSF matrix and RP domains, and there was a significant amount of Fe^{2+} in the domain. STEM core-loss EELS analysis of the LSF matrix (blue curve in Fig. S5c) and domain boundary (green curve) revealed a decrease in the Fe L_{23} signal and an increase in the La M_{45} signal in the domain boundary. Comparison of the Fe L_{23} EELS near-edge fine structure measured in the LSF and in the domain boundary revealed a 1-eV shift of the Fe L_3 peak (~ 704 eV) to lower energy loss in the domain, indicative of appreciable Fe reduction from 3+ to 2+ (Fig. S5c).